Bio-Design and Manufacturing (2021) 4:171–189
https://doi.org/10.1007/s42242-020-00111-6

RESEARCH ARTICLE

A biomimetic basement membrane consisted of hybrid aligned nanofibers and microfibers with immobilized collagen IV and laminin for rapid endothelialization

Chenglong Yu[1,2,3,4] · Guoping Guan[1,2] · Stefanie Glas[3,4] · Lu Wang[1,2] · Zhutong Li[3,4] · Lih-Sheng Turng[3,4]

Received: 18 September 2020 / Accepted: 7 November 2020 / Published online: 3 January 2021
© Zhejiang University Press 2021

Abstract

Rapid formation of a continuous endothelial cell (EC) monolayer with healthy endothelium function on the luminal surface of vascular implants is imperative to improve the longtime patency of small-diameter vascular implants. In the present study, we combined the contact guidance effects of aligned nanofibers, which enhance EC adhesion and proliferation because of its similar fiber scale with native vascular basement membranes, and aligned microfibers, which could induce EC elongation effectively and allow ECs infiltration. It was followed by successive immobilization of collagen IV and laminin to fabricate a biomimetic basement membrane (BBM) with structural and compositional biomimicry. The hemolysis assay and platelet adhesion results showed that the BBM exhibited excellent hemocompatibility. Meanwhile, the adhered human umbilical vein endothelial cells (HUVECs) onto the BBM aligned along the orientation of the microfibers with an elongated morphology, and the data demonstrated that the BBM showed favorable effects on EC attachment, proliferation, and viability. The oriented EC monolayer formed on the BBM exhibited improved antithrombotic capability as indicated by higher production of nitric oxide and prostacyclin (PGI2). Furthermore, fluorescence images indicated that HUVECs could infiltrate into the BBM, implying the BBM's ability to enhance transmural endothelialization. Hence, the BBM possessed the properties to regulate EC behaviors and allow transmural ingrowth, demonstrating the potential to be applied as the luminal surface of small-diameter vascular implants for rapid endothelialization.

Keywords Biomimetic basement membranes · Aligned electrospun fibers · Surface modification · Endothelialization · Anti-thrombogenicity · Transmural ingrowth

Introduction

Vascular transplantation is the most effective means of treating severe cardiovascular diseases. However, the limited availability of healthy and mechanically robust autologous, allogenic, or xenogeneic vein sources has stimulated the development of artificial vascular implants [1, 2]. Polyethylene terephthalate (PET), polytetrafluoroethylene (PTFE), and other commercial polymers have been successfully utilized for large-diameter (inner diameter >6 mm) artificial blood vessel replacements. However, due to the disappointing long-term patency caused by the intimal hyperplasia and high risk of luminal thrombosis, there has not been a successful commercial small-diameter (inner diameter <6 mm) vascular graft so far [3–5]. The innermost layer of native blood vessels is the endothelium, which is consisted of a continuous monolayer of endothelial cells (ECs) that are in direct contact with blood, participating in multi-faceted blood

✉ Guoping Guan
ggp@dhu.edu.cn

✉ Lih-Sheng Turng
turng@engr.wisc.edu

1 Key Laboratory of Textile Industry for Biomedical Textile Materials and Technology, College of Textiles, Donghua University, 2999 North Renmin Road, Songjiang District, Shanghai 201620, China

2 Engineering Research Center of Technical Textiles of Ministry of Education, College of Textiles, Donghua University, Shanghai 201620, China

3 Wisconsin Institute for Discovery, University of Wisconsin-Madison, 330 North Orchard Street, Madison, WI 53715, USA

4 Department of Mechanical Engineering, University of Wisconsin-Madison, 1513 University Ave, Madison, WI 53706, USA

vessel activities, such as inflammation, fibrinolysis, hemostasis, and extracellular matrix (ECM) production [1, 6, 7]. Importantly, the endothelium could act as an anti-coagulation barrier to prevent thrombus formation by inhibiting platelet adhesion [8, 9]. Unfortunately, artificial vascular grafts cannot realize rapid endothelialization in situ because of the low EC initial attachment as well as cell spreading and growth [10–12]. Therefore, enhancing the endothelialization of artificial vascular grafts has become an active research for the vascular tissue engineering development [13–15].

In vivo, ECs attach on vascular basement membranes (BMs), and the native BMs exhibit a complex meshwork topography with nanoscale range (1–100 nm) fibers and submicron range (100–1000 nm) pores [16]. Collagen IV and laminin are always contained in BMs, working together with elastin and other functional components to provide the vital physical support for vascular endothelium [17–19], as well as some special signals to surrounding cells and tissues [16, 19–22]. They could help maintain the anti-thrombotic property of the EC monolayer [23, 24] and regulate various cell surface interactions, leading to discrepant promotion of different EC behaviors [25]. Genge et al. [12] compared the effects of different components of ECM on human umbilical vein endothelial cell (HUVEC) behaviors, and they found that HUVECs exhibited the best adhesion and proliferation on laminin-coated substrates when compared to gelatin- or fibronectin-coated samples. After exposed to shear stress, the HUVECs cultured on laminin and ECM showed similar cell densities and the stress fiber patterns, meaning that the vascular implants coated with laminin might enhance the shear stress resistance property of ECs. According to the study of Palotie et al. [26], bovine aortic ECs attached more preferably to the surfaces modified with fibronectin, collagen III, and collagen IV than with laminin and collagen I and collagen V. Form et al. [27] reported that the proliferation of bovine aortic ECs was remarkably faster on laminin than on collagen IV.

Additionally, ECs in vivo also exhibit an elongated morphology and align along the direction of blood flow because of the flow-mediated mechanotransduction effects, which could lead to cytoskeletal rearrangement and paralleled stress fiber bundles [28–30]. Of note, researchers had revealed that the monolayer of oriented ECs played crucial roles in regulating anti-thrombogenic and pro-inflammatory reactions [23, 24, 31, 32], while showing preferable shear stress resistance and low flow disturbance [33, 34]. Given the advantages of elongated ECs, the grooved surfaces and the aligned electrospun fibers have always been employed to regulate the alignment of ECs. Note that the structure parameters of grooves, as well as the diameters and orientation degrees of electrospun fibers would affect ECs activities differently [1, 24, 32, 34–38]. Li et al. [39] evaluated the HUVEC behaviors on electrospun substrates with different fiber diameters and orientations, and they found that nanosized fibers could enhance EC adhesion and proliferation remarkably. Based on our previous studies [40, 41], the adhesion and proliferation of ECs were significantly improved on nanoscale electrospun membranes, whose fiber diameters were close to that of the native BMs (within 100 nm), while ECs presented a more elongated morphology on membranes with micro-aligned fibers than with nano-aligned fibers. In addition, the aligned electrospun microfibers with diameter of 2.738 μm had the strongest contact guidance effects on HUVEC elongation, and the HUVECs infiltrated into the membrane, demonstrating its capability for improving transmural ingrowth endothelialization [42, 43]. As reported earlier, besides transanastomotic outgrowth and fallout of blood-borne cells endothelialization mechanisms, transmural ingrowth endothelialization has been described as a main modality of endothelialization, provided that the porosity, pore size, and permeability of vascular grafts are adequate to allow capillary ingrowth and transport of angiogenic factors [42–44]. Pennel et al. had confirmed that the transmural capillary ingrowth was essential for confluent vascular graft healing [44], which could occur independently from the transanastomotic endothelialization [45]. Adjusting the grafts structures [46, 47] and chemical grafting [44, 48] have both been studied to improve cell infiltration for transmural capillary ingrowth.

In the present study, we developed a biomimetic basement membrane (BBM) structurally and compositionally, which was aimed at optimizing the endothelialization process of small-diameter vascular implants. Aligned polycaprolactone (PCL) electrospun nanofibers with diameter of 73 nm were utilized to mimic the nanoscale feature of native BMs, and aligned microfibers with diameter of 2.7 μm were electrospun simultaneously, collecting two kinds of fibers together to develop the hybrid structure of the BBMs [41]. The resulting BBMs could combine the advantages of both aligned nanoscale fibers on EC adhesion and proliferation, as well as aligned micro-scale fibers on EC orientation and penetration. Furthermore, collagen IV and laminin as the main components of native BMs were successively immobilized through 1-ethyl-3-(3-dimethylaminopropyl) carbodiimide hydrochloride (EDC)/*N*-hydroxysuccinimide (NHS) coupling chemistry to realize biomimicking the BMs not only structurally but compositionally. A series of characterization tests had been carried out to evaluate the performances of the BBMs.

Materials and methods

Materials

Polycaprolactone (PCL, Mn ~ 80 kDa) was obtained from Sigma-Aldrich (USA). Trichloromethane (CHL) and acetic acid (AA) were purchased from Lingfeng Chemical Reagent Co., Ltd. (China). Formic acid (FA) and alcohol were supplied by Sinopharm Chemical Reagent Co., Ltd. (China). Bovine serum albumin (BSA) and BCA Protein Assay Kits were obtained from Sangon Biotech. (China). Human umbilical vein endothelial cells and human Endothelial Cell Medium kit (Catalog#1001) were purchased from ScienCell Research Laboratories (USA). Porcine whole blood with Na citrate and RPMI-1640 medium were bought from Fisher Scientific (USA). Cell counting kit-8 (CCK-8) was supplied by MedChemExpress (USA). Nitrite assay kit was purchased from BioVision (USA), and Prostacyclin ELISA kit was obtained from Enzo Life Sciences (USA). Rhodamine phalloidin and 40, 6-diamidino-2-phenylindole (DAPI) were purchased from Yeasen Biotechnology Co., Ltd. (China). Live/Dead viability kit was supplied by Biotium (USA). The water used in the present study was purified by a Milli-Q system (Millipore, USA). All the chemicals were of analytical grade and were used without further treatment unless specially mentioned.

Fabrication of the BBMs

Through electrospinning, the aligned electrospun nanofibers and microfibers were collected simultaneously to develop the structure of the BBM. As discussed before [41], electrospun solutions were prepared by dissolving PCL for 24 h at room temperature in a mixed solvents of formic acid and acetic acid (7:3 v/v) at a concentration of 10 wt%, and chloroform and ethanol (7:3, v/v) at 20 wt% for the fabrication of 73 nm sample and 2.7 μm sample, respectively. A roller collector was used to fabricate aligned fibers, and the rotator speed was set as 1500 rpm (10 m/s). For 73 nm sample preparation, the flow rate was controlled at 0.1 mL/h. The distance between the needle tip and the collector was 17 cm, and the voltage was 20 kV. For electrospinning of 2.7 μm sample, the flow rate, spinning distance, and high voltage were set as 2 mL/h, 20 cm, and 20 kV, respectively. The as-fabricated scaffolds were cleaned and wetted in 70% (v/v) ethanol solution, then washed with deionized water. The sample was named the StrM, meaning it only mimicked the structure of native BMs. As shown in Fig. 1, the StrM was incubated in 0.4 M NaOH solution for 20 min at 40 °C, aiming to activate the surface because of the bioinert properties of PCL. Surface hydrolysis by NaOH solution is facile for modifying biodegradable polymeric materials such as PCL [49]. After NaOH treatment, the activated-StrM was immerged in 2-(*N*-Morpholino) ethanesulfonic acid (MES) solution (0.1 M, pH 5.0) containing 5 mg/mL EDC and 5 mg/mL of NHS for 1 h at 25 °C, then submerged in collagen IV solution (100 μg/mL in 0.5 M acetic acid) for 2 h at 25 °C, followed by rinsed with 0.5 M acetic acid and phosphate-buffered saline (PBS) to remove the unreacted collagen IV. The resultant sample was named the COL-StrM. Afterwards, the COL-StrM was soaked in the above EDC/NHS solution for 1 h at 25 °C, then reacted with laminin (20 μg/ml in PBS, containing 0.15 M NaCl, pH 7.4) for 2 h at 25 °C. The prepared sample was washed 3 times with PBS and named the BBM. We also prepared the LAM-StrM sample by immobilizing laminin onto the activated-StrM through EDC/NHS coupling chemistry as described above.

General characterization

The morphologies of the various samples were observed by a scanning electron microscope (SEM, SU8010, Hitachi, Japan), and the acceleration voltage was 15 kV. The fiber alignment of different samples was evaluated using the obtained SEM images and Image J software as described in a previous study [35]. The 3D images and the force–distance curves of the adhesion force of different samples were generated by an atomic force microscope (AFM, 5500 AFM-SPM, Keysight, USA) with contact mode, and a 960 nN original approach force was applied to obtain the force–distance curves. Furthermore, arithmetic mean roughness (Sa) was calculated with analyzing software (Pico Image Elements 7.3), representing the arithmetic average of the absolute values of the profile height deviations from the mean line within the evaluation length. The contact angle instrument (OCA15EC, Dataphysics, Germany) was applied to measure the wettability of samples, and PBS solution rather than water was chosen for the measurement in the present study. The contact angles were obtained after the droplets contacted with the surfaces for 15 s. Fourier transform infrared (FTIR) spectra were recorded using a FTIR Spectrometer (Nicolet 6700, Thermo Fisher Scientific, USA) in the range of 3800–600 cm^{-1} to identify the functional groups in the different samples, with a resolution of 4 cm^{-1}. X-ray photoelectron spectroscopy (XPS) analyses were performed on an ESCALAB 250Xi (Thermo Fisher Scientific, USA) spectrometer to examine the surface atomic composition.

Bovine serum albumin (BSA) adsorption

BSA adsorption was assessed utilizing a simplified method. Briefly, the samples were cut into discs (14 mm in diameter) and placed in separate wells of 24-well culture plates, then sterilized with 75% (v/v) ethanol solution and rinsed in PBS solution three times. 1 mL BSA solution (1 mg/mL) was injected into each well, followed by incubated the samples

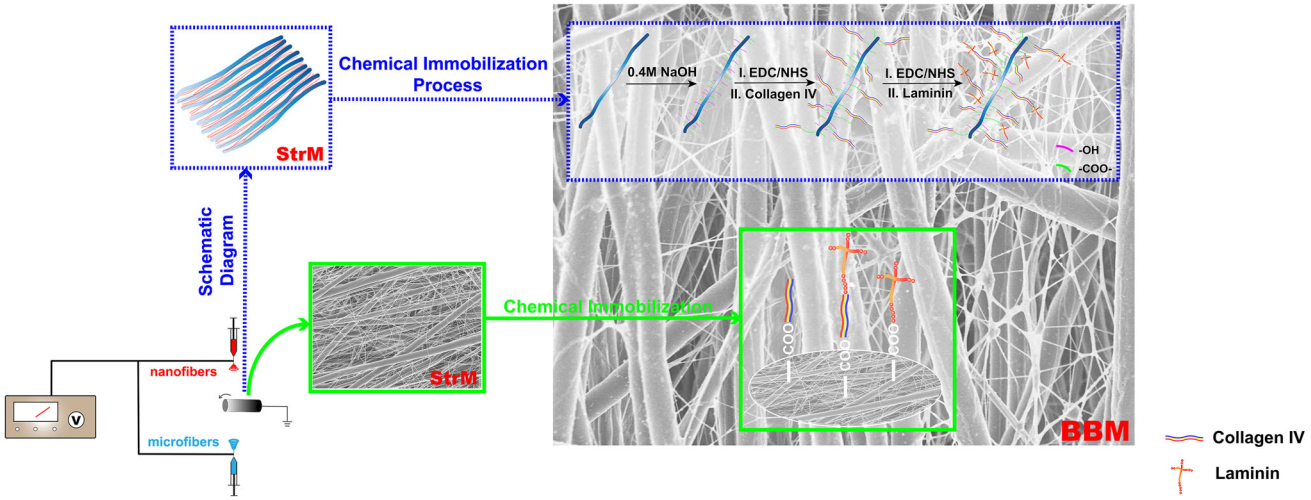

Fig. 1 Schematic illustration of the BBM preparation process

in a shaker for 6 h at 37 °C. In the present study, we measured the absorbance of the supernatant after adsorption test to evaluate the BSA adsorption results using a BCA protein assay kit, rather than the actual amounts of adsorbed protein on different samples.

Hemocompatibility evaluation

Hemolysis assay in vitro

For hemolysis rate test, the detailed procedures were performed following a previous method [50]. Briefly, each sample (10 mg) was incubated in 10 mL PBS for 72 h at 37 °C. Afterwards, 0.2 mL diluted blood (porcine whole blood was diluted with PBS with a volume ratio of 4:5) was added to each sample followed by incubation for 1 h at 37 °C. Then, the absorbance of the supernatants, which were obtained after centrifugation at 800×*g* for 5 min, was measured at 545 nm using an ultraviolet spectrophotometer. Hemolysis rate (HR) was calculated following Eq. (1), and 10 mL distilled water (positive control) and 10 mL PBS (negative control) were applied for comparison, respectively.

$$\mathrm{HR}(\%) = \frac{\mathrm{OD_{SA}} - \mathrm{OD_{NE}}}{\mathrm{OD_{PO}} - \mathrm{OD_{NE}}} \times 100 \quad (1)$$

where $\mathrm{OD_{SA}}$ is the absorbance of experimental sample, $\mathrm{OD_{PO}}$ represents the absorbance of positive control, and $\mathrm{OD_{NE}}$ represents the absorbance of negative control.

Platelet adhesion

The quantities and morphologies of platelets were investigated to evaluate the anti-thrombogenicity of different samples. We centrifuged the anti-coagulated porcine blood at 1500 rpm for 15 min at room temperature to obtain platelet-rich-plasma (PRP) [51]. For the platelet adhesion test, samples were incubated in PBS for 1 h at 37 °C firstly. After that, 500 μL PRP was added onto sample surfaces cautiously and then incubated at 37 °C for 2 h, followed by rinses with PBS three times to wash away weakly adhered platelets. The adhered platelets were submerged in 4% paraformaldehyde at 4 °C for 1 day. Finally, samples were dehydrated with a series of ethanol solution (50%, 70%, 80%, 90%, and 100%, v/v) and dried in a vacuum drying oven before SEM observation.

Cell culture

Before cell seeding, all samples were cut into round pieces and placed in separate wells of 24-well culture plates, then sterilized by 75% (v/v) ethanol solution and rinsed with PBS three times. HUVECs were seeded onto samples at a density of 4×10^4 cells per well for cell adhesion analysis, 1×10^4 cells per well for all other tests, and maintained in the supplied human Endothelial Cell Medium. All cells were incubated at 37 °C in a humidified 5% CO_2 atmosphere. The cell culture medium of the NO and PGI2 production evaluation groups was not changed until testing at 3 day, and the culture medium was replaced every 2 days for all other tests.

Biological characterization

HUVEC adhesion and proliferation

To evaluate cell adhesion, the HUVECs were stained at 6 h after sufficient rinse to wash away the floating cells. Briefly, HUVECs cultured on different samples were fixed with 4% paraformaldehyde at 37 °C for 30 min firstly, then washed

with PBS three times and permeabilized using 0.5% Triton X-100 (in PBS) for 10 min, followed by incubated in 1% BSA (in PBS) for 20 min to weaken the nonspecific background staining. The following fluorescent staining process was conducted away from light. For the cytoskeleton staining, the cells were stained with rhodamine phalloidin for 30 min at room temperature and then rinsed with PBS three times. After that, the cells were stained with DAPI for nucleus staining at room temperature for 2 min, followed by PBS washing three times again. Samples were observed using a fluorescence microscope (DMI3000, Leica, Germany). The actual numbers of HUVECs on different samples were counted and transferred to cell adhesion densities for evaluation.

CCK-8 assay was utilized to assess HUVEC proliferation at days 1, 3, and 5, respectively. Briefly, the culture medium was removed and the samples were rinsed gently three times using PBS firstly, then 50 μL CCK-8 solution mingled in 450 μL RPMI-1640 medium was added per well. After incubated in incubator (37 °C, 5% CO_2) for 2 h, the amounts of HUVECs were determined by the optical absorbance values at 450 nm using a microplate reader (MULTISKAN FC, Thermo Fisher Scientific, USA).

HUVEC viability (Live/Dead assay)

The HUVEC viability was determined by the numbers of living and dead cells at 5 day, using a Live/Dead viability kit. Briefly, the culture medium in the wells was removed firstly, followed by washing the samples carefully with PBS, then adding staining solution onto the samples according to the instructions. Next, the samples were incubated at room temperature for 30 min prior to the cell observation with a fluorescence microscope (DMI3000, Leica, Germany). The Live/Dead viability kit contained green fluorescent Calcein AM to image the cytoplasm of living cells, and red fluorescent propidium iodide to view dead cells. For determining the percentages of live and dead cells on the different samples, dead cell controls, healthy cell controls, and cell-free controls were prepared, respectively, followed by staining cells, and measuring fluorescence of experimental and control samples. The percentages of live and dead cells could be calculated from the fluorescence readings as described in the provided protocols.

HUVEC morphology

HUVECs cultured on different samples were stained as described earlier for observation, and the morphologies of cells were characterized using Image J software. The value of the major axis/minor axis of nuclei of HUVECs (fitted to ellipses) was defined as the aspect ratio [41]. Based on previous study [52], nuclear shape index (NSI) was calculated as below:

$$\mathrm{NSI} = \frac{4\pi \times \text{area}}{\text{perimeter}^2} = \frac{2LW}{L^2 + W^2} \tag{2}$$

where L and W are half of the values of nuclear length and width, respectively.

Nitric oxide (NO) production of HUVECs

NO released by the healthy endothelium could act as an anti-thrombogenic agent, also the anti-proliferative agent for smooth muscle cells [8, 53, 54]. In the present study, the amounts of NO released in the culture media of HUVECs cultured on different samples were assessed using the Nitric Oxide Assay kit after 3 day culture. To eliminate the variation due to cell proliferation, the measured NO production was finally normalized by the cell number.

Prostacyclin (PGI2) production of HUVECs

PGI2 could help maintain the balance of anti-thrombosis and anti-coagulation in vivo [24, 55]. HUVECs were cultured on different samples for 3 days, and then, the culture medium was collected for the measurement of the concentration of PGI2 using a PGI2 ELISA Kit, according to the manufacturer's instructions. To eliminate the variation due to cell proliferation, the measured PGI2 production was finally normalized by the cell number.

Statistical analysis

All results were presented as mean values ± standard deviation. One-way analysis of variance (ANOVA) and LSD test were used to statistically analyze the significant differences between groups using SPSS software (version 16.0). Differences were accepted as significant when $P < 0.05$(*), $P < 0.01$(**) and $P < 0.001$(***).

Results and discussion

Surface chemistry

Aligned electrospun scaffolds without further chemical modifications were all prepared using the raw PCL material in the present study, suggesting their same chemical properties. Therefore, we only used the nano/microfibrous scaffold for the FTIR and XPS characterizations, and named it as PCL. As shown in Fig. 2a, carbonyl group vibration at 1730 cm^{-1}, –C–O–C– vibrations at 1186 and 1241 cm^{-1}, as well as -CH_2- bending vibrations at 1366, 1418, and

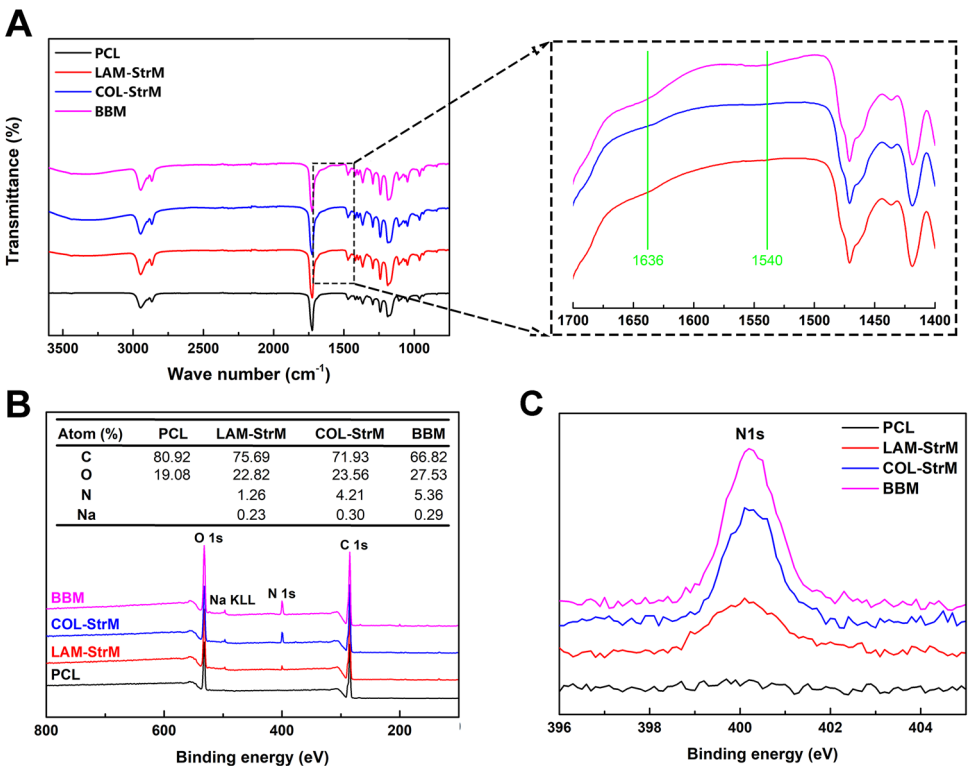

Fig. 2 FTIR spectra (**a**) and XPS analysis (**b**) of different samples; **c** XPS spectra for N1s

1471 cm^{-1}, respectively, could be observed in all spectra, as these were the characteristic peaks of PCL. After biomolecule immobilization, there were three distinct peaks that could be identified in the COL-StrM, the LAM-StrM, and the BBM spectra. The new peaks appearing at 1636 cm^{-1} and 1540 cm^{-1} represented the amide I and amide II peaks, respectively, indicating the successful immobilization of proteins in the present study. Furthermore, a band at 3000–3600 cm^{-1} could be observed, corresponding to the stretching of –OH, or –NH– groups of collagen IV and laminin.

XPS was employed to further characterize the atomic or chemical composition of the sample surfaces. In Fig. 2b, we could found that only C and O were detected on PCL spectrum, appearing at binding energies of 285 eV and 532 eV, respectively. After biomolecule immobilization, an additional N peak at binding energy of 399 eV was detected on the COL-StrM, LAM-StrM, and the BBM spectra, which originated from the collagen IV and laminin and provided direct evidence for the successful protein immobilization. Of note, from the atomic percentage statistical data (inserted table in Fig. 2b), the higher biomolecule concentration contributed to the higher N intensity of the COL-StrM (4.21%), when compared to the LAM-StrM (1.26%). Note that the applied biomolecule concentrations and immobilization efficiency both led to the difference on N intensity, although the accurate immobilization efficiencies of collagen IV and laminin need further study. Moreover, the BBM exhibited the highest N intensity of 5.36%, which was attributed to the immobilization of both collagen IV and laminin. The same conclusion could also be drawn from the N peaks in Fig. 2c. Our previous study had confirmed that the grafting method applied in the present study could realize the successful biomolecule immobilization [40].

Surface morphology

The SEM and AFM graphs of different samples are shown in Figs. 3a and 4, respectively. Figure 3b presents the distributions of fiber diameters of the 73 nm and 2738 nm samples, and the normalized radial intensity results from Fig. 3c showed the greatest intensity along a single axis corresponding to the direction of fiber orientation for all samples. In Fig. 3a, it could be seen that the samples with aligned nanofibers and microfibers had relatively smooth surfaces, as well as the StrM, which was composed of aligned nanofibers and microfibers. The surface roughness of the 2738 nm sample, as measured by the AFM, was 1.15 ± 0.16 μm, much higher than 0.13 ± 0.012 μm of the 73 nm sample because of its thicker fibers. For the StrM, the presence of nanofibers and microfibers contributed to a medium roughness value of 0.54 ± 0.053 μm (Fig. 4). After collagen IV immobilization, there were nanoscale features on the surfaces of the fibers, and the fiber surfaces became rough. Similar situations could also be seen on the fiber surfaces of the LAM-StrM, although no obvious differences could be found between the

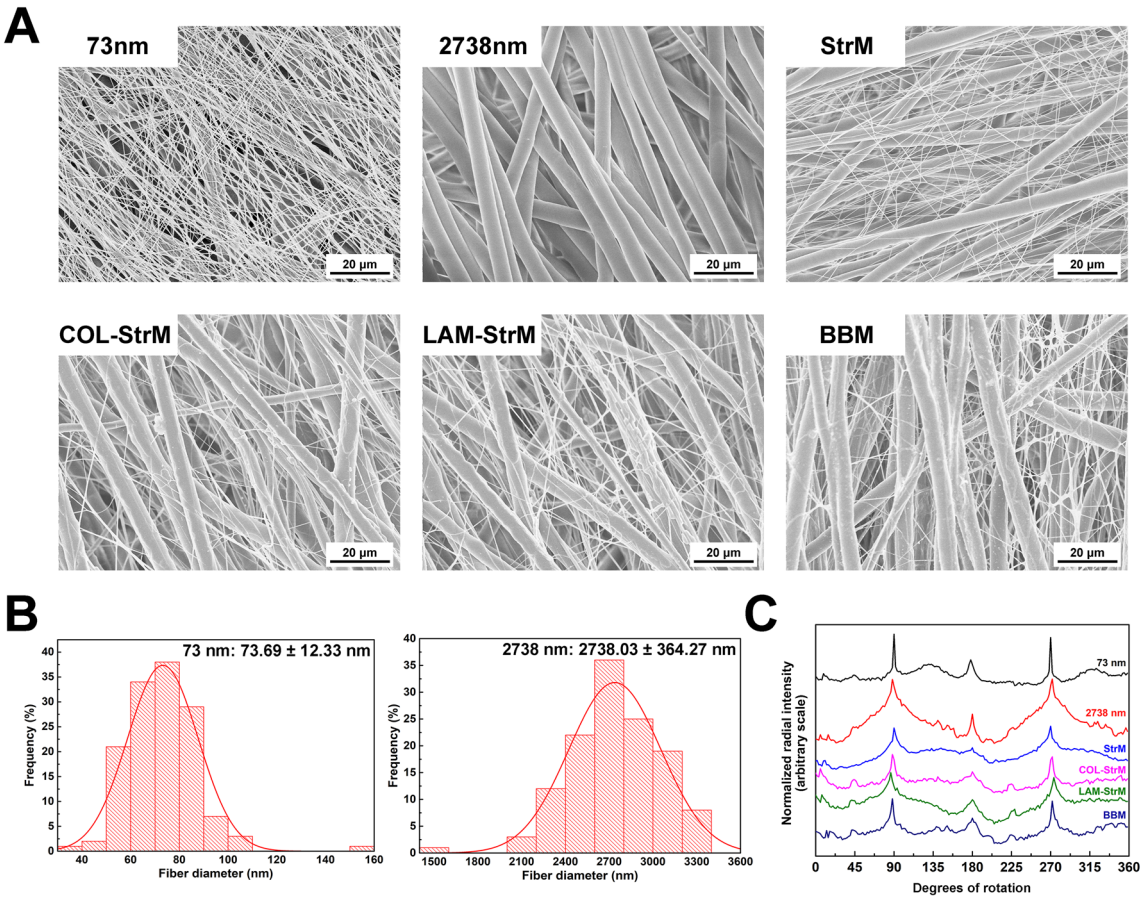

Fig. 3 **a** SEM photographs of different samples; **b** distributions of fiber diameters of the 73 nm and 2738 nm samples; **c** normalized radial intensities against degrees of rotation

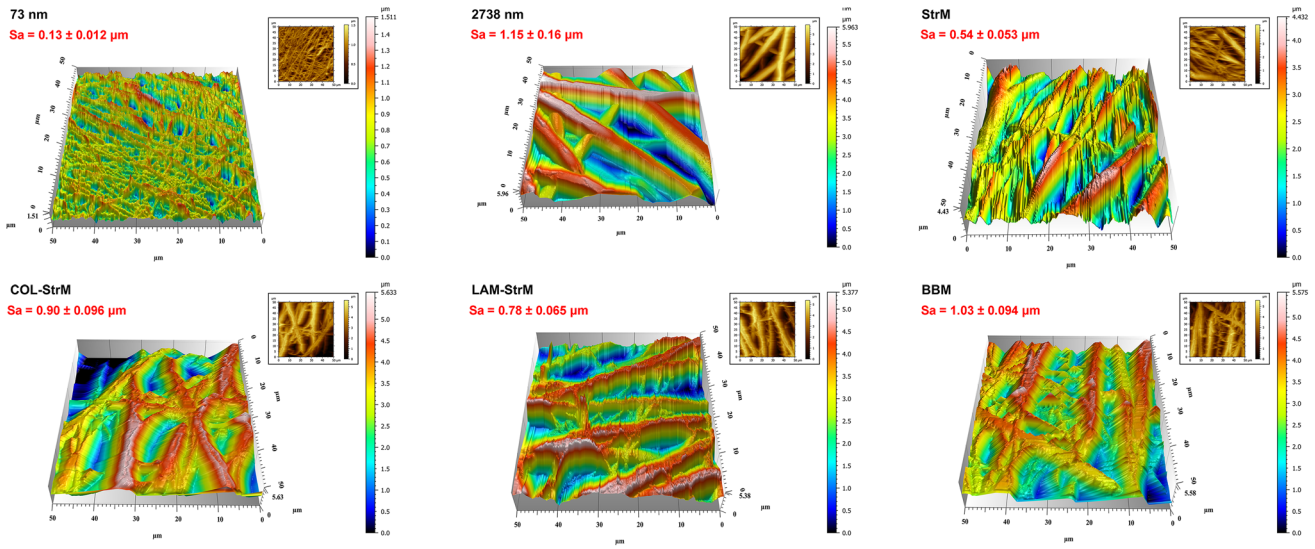

Fig. 4 Topography and surface roughness (Sa) of different samples measured by the AFM

COL-StrM and the LAM-StrM from Fig. 3a. However, there was indeed difference between their roughness values (cf. Fig. 4, the COL-StrM of 0.90 ± 0.096 μm and the LAM-StrM of 0.78 ± 0.065 μm) because of different immobilized biomolecules and applied biomolecule concentrations. After immobilizing both collagen IV and laminin, we could find

that there were more aggregates on the fiber surfaces of the BBM than the COL-StrM and the LAM-StrM from Fig. 3a, and the roughness value of the BBM increased to 1.03 ± 0.094 μm.

Adhesion force measured by AFM

AFM could be used to assess the adhesion force through the force–distance curves, which were obtained by controlling AFM tips retraction after direct contact with the sample surfaces [56–59]. As shown from the schematic illustration in Fig. 5a, the negative force at the retraction process of the force–distance curve indicated the adhesion force. The comparisons between different samples were discussed by statistically analyzing the adhesion force values of several random locations on the sample surfaces. In Fig. 5b, it was found that the average adhesion force of the 73 nm sample was 921.60 ± 361.19 nN, much higher than that of the 2738 nm sample (518.40 ± 99.36 nN). This result is in agreement with the observation of Li et al. who found that the thinner fibers constrained harder force to the water, AFM tips, and fibroblast cells [59]. After collagen IV and laminin immobilization, two separate adhesion force distributions could be obtained, and they represented the adhesion forces of nanofibers and microfibers, respectively. For the COL-StrM, the average adhesion forces of nanofibers and microfibers were 3192.66 ± 699.19 nN and 605.18 ± 268.68 nN, while the LAM-StrM demonstrating 2286.72 ± 151.78 nN and 605.41 ± 166.39 nN, respectively. Comparing the changes of adhesion forces, we found that the biomolecules affected the nanofibers much more significantly than microfibers. The adhesion forces of nanofibers increased 3.46 times for the COL-StrM and 2.48 times for the LAM-StrM, while only approximate 1.17 times for microfibers of both the COL-StrM and the LAM-StrM whose adhesion force values were similar. Besides the inherent differences between collagen IV and laminin on adhesion force, the immobilization amount of biomolecules might also contribute to the different adhesion forces. In the present study, the immobilization concentrations of collagen IV and laminin used were 100 μg/mL and 20 μg/mL, respectively, and the adhesion force of nanofibers responded appreciably to the concentration difference because of its fine diameter, while the diameters of microfibers were too large to show the effect of immobilized biomolecules. Of note, for the COL-StrM and the LAM-StrM, the similar adhesion force values of microfibers but different biomolecule immobilization concentrations suggested that laminin could improve the adhesion force more effectively than collagen IV. For the BBM, the average adhesion forces of nanofibers and microfibers were both the highest among all the samples, increasing 3.64 times to 3352.92 ± 943.77 nN and 1.71 times to 888.48 ± 598.42 nN, respectively. This suggested that combining collagen IV and laminin together for immobilization could further enhance the adhesion forces. More importantly, higher adhesion force corresponded to higher surface energy and drag tension force. When applied to cell incubation, it was expected that ECs could attach more stably on the BBM [59]. In human body, ECs adhered onto the inner surface of vascular implants are always subject to physiological flow conditions, and the ECs may be sloughed off from the surfaces if the adhesion strength is not strong enough [31, 60].

Surface wettability and BSA adsorption

As shown in Fig. 6a, the 73 nm sample showed the highest PBS contact angle of $133.15 \pm 1.91°$, much higher than that of the 2738 nm sample ($120.05 \pm 0.16°$). Similar results had also been observed by Ghobeira et al., who reported that the water contact angles of aligned electrospun fibers gradually decreased with increase in fiber diameters [61]. Previous studies indicated that the high packing density of the aligned fibers tended to form roughness creases instead of well delineated pores, thus leading to less air entrapment [61, 62]. Though the fiber adhesion force of the 73 nm sample was higher than that of the 2738 nm in the present study (Fig. 5b), we speculated that the effect of surface topography on PBS droplets penetration was significant enough to counteract the opposite and competing effects of surface energy and fiber adhesion force. For the StrM, the existence of both thick and fine fibers led to a looser structure and larger gaps than the 73 nm and 2738 nm samples, resulting in the fast and efficient PBS droplets infiltration into the membranes within 15 s. For the COL-StrM, LAM-StrM, and BBM, besides the similar structure with the StrM, hydrophilic collagen IV and laminin would also contribute to the PBS penetration. Furthermore, the hydrolization of the hydrophobic O=C–O– groups of PCL led to the increase in hydrophilic groups on the fiber surfaces, such as –COO– and –OH [40], further facilitating the PBS droplets infiltration.

In Fig. 6b, we could find that the 73 nm sample showed the lowest absorbance value, indicating its highest BSA adsorption according to our experiment design. As for BSA, it belongs to the albumin protein group and helps to decrease platelet adhesion [63]. In addition, several studies demonstrated that the albumin was more likely to adhere to hydrophilic surfaces [64, 65]. Although the 73 nm sample exhibited the highest PBS contact angle among all the samples and its similar nanoscale dimensions with proteins might restrict protein adsorption, the dominant effect of the largest surface area (because of the finest fiber diameter) contributed to its highest BSA adsorption amount [66]. The amount of BSA adsorption on the 2738 nm sample was slightly less than that of the 73 nm, but with no significant difference. Compared with the 73 nm and the 2738 nm samples, the looser

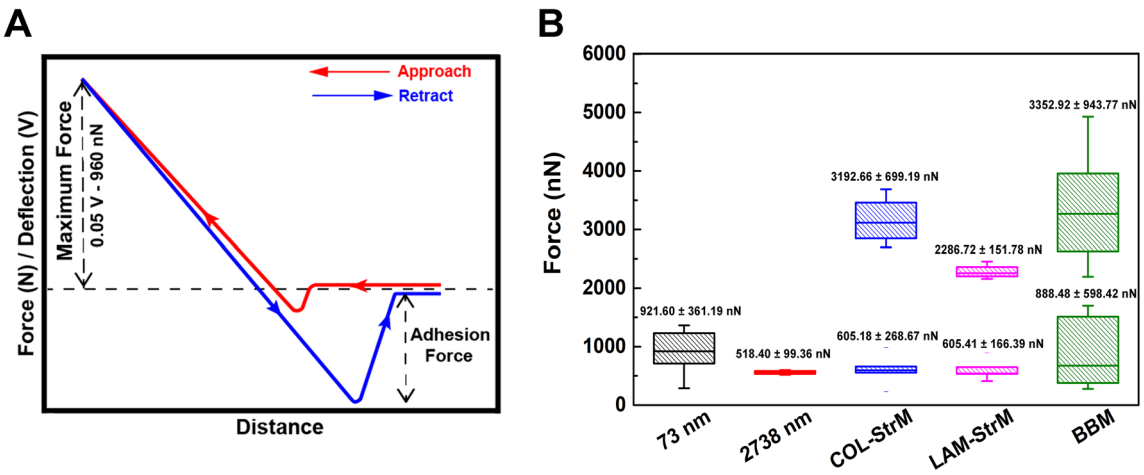

Fig. 5 **a** The typical force–distance curve; **b** statistical results of the adhesion force

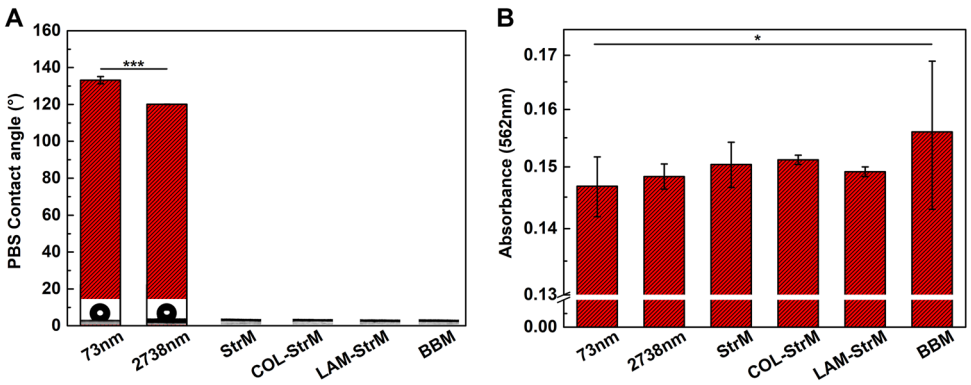

Fig. 6 **a** PBS contact angles of different samples; **b** the absorbance values corresponding to the amount of remaining BSA in solutions after tests

structure and larger gaps of the StrM led to limited surface area, resulting in less BSA adsorption. After collagen IV and laminin immobilization, the COL-StrM and the LAM-StrM showed comparable BSA adsorption with the StrM. It was speculated that the biomolecule immobilization had limited influences on BSA adsorption, and the relatively low grafting concentrations employed in the present study might be the reason for that. The BBM exhibited the lowest BSA adsorption amount, which was significantly less than that of the 73 nm sample ($P < 0.05$).

Hemocompatibility evaluation

For blood-contacting biomaterials, hemocompatibility is one of the essential indicators to evaluate the suitability of them for in vivo applications. In the present study, the hemolysis rate and platelet adhesion tests were performed for evaluation. Hemolysis of erythrocytes is a crucial index for evaluating blood compatibility of materials, and it should be less than 2% to meet the requirements for biomaterials being implanted into the human body [50, 67]. As shown in Fig. 7a, no obvious hemolysis phenomenon could be observed from the inset photograph. Except for the 73 nm sample ($2.12 \pm 0.59\%$), the hemolysis rates of other samples were all less than 2%, suggesting that these samples could be considered acceptable as nonhemolytic materials. Of note, the hemolysis rates of the COL-StrM, LAM-StrM, and BBM were less than 0, indicating that they nearly did not cause red blood cell rupture when compared with negative control. It was because of the satisfactory biocompatibility of collagen IV and laminin [13, 68].

The adhesion and activation of platelets on the luminal surfaces of vascular grafts will trigger blood coagulation and thrombus formation, leading to the implantation failures [5, 69, 70]. In Fig. 7b, c, we could find that significantly more platelets adhered on the 73 nm sample when compared with the 2738 nm sample. The StrM exhibited the largest value, significantly higher than all other samples. Of note, the adhered platelets on the 73 nm, the 2738 nm, and the StrM showed a dendritic morphology with many extruding filopodia (Fig. 7c). Previous study has showed that platelets forming primarily filopodia may recruit other platelets [71]. For the COL-StrM, LAM-StrM, and BBM, they showed similar amounts of adhered platelets, with no significant differences.

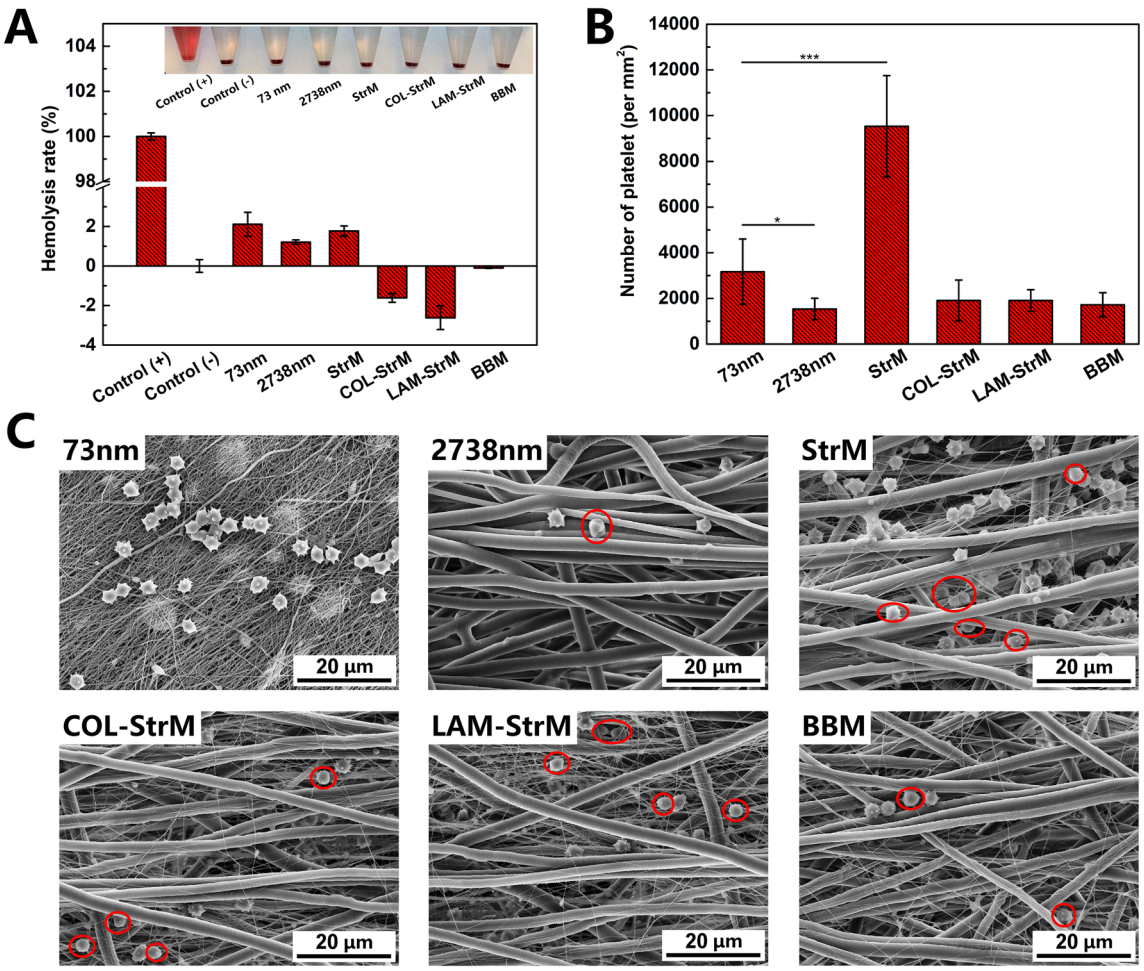

Fig. 7 **a** Hemolysis rates of different samples; **b** number of platelets adhered on different samples; **c** SEM images of adhered platelets. Round platelets were marked with red circles

It is well known that the increase in hydrophilicity was correlated with the decrease in platelet adhesion and activation [3, 72]. Compared with the 2738 nm sample, the PBS contact angle of the 73 nm sample was significantly higher (cf. Fig. 6a). In addition, the larger surface area of the 73 nm sample might also contribute to higher number of platelets adhered [41]. As discussed earlier, the drag tension force of the 73 nm sample was higher than that of the 2738 nm sample, suggesting the greater force and attraction of the 73 nm sample to the platelets, which is in agreement with Li et al. [59]. For the StrM, it showed the largest amount of adhered platelets, up to 9533 ± 2213 platelets/mm^2. The StrM was composed of both nanofibers and microfibers, and the nanofibers filled up the large gaps between microfibers and restricted the platelets penetration when compared with the 2738 nm sample. During the evaluation process, we needed to wash away the weakly adhered platelets. The porous surface of the StrM resulting from its structure was more likely to collect the floating and weakly adhered platelets than the 73 nm sample. Although the topographical cues of the StrM and the lack of biomolecule immobilization might be the main reasons for the largest number of adhered platelets, intensive and elaborate explorations are still required to prove this hypothesis.

Collagen IV and laminin were both adhesion biomolecules, which had the binding sites of the platelets and could cause platelet adhesion, activation, and aggregation [73, 74]. Howbeit, the statistical results shown in Fig. 7b indicated that the numbers of adhered platelets on the COL-StrM, LAM-StrM, and BBM were significantly lower than that on the StrM. Moreover, among the adhered platelets, some platelets showed round shape (marked in red circles in Fig. 7c) with less filopodia, indicating that they generally had a low attachment force to the surfaces [71]. Here, we speculated that the biomolecule immobilization process changed the original platelet adhesion and activation properties of both collagen IV and laminin, leading to the decreased number of adhered platelets. Furthermore, the fiber surfaces of the COL-StrM, LAM-StrM, and BBM were more hydrophilic than that of the StrM because of the

hydrophilicity of biomolecules, leading to more albumin adsorbed which contributed to less adhered and activated platelets. In addition, since the adsorption and interaction of albumin on hydrophilic and hydrophobic surfaces were different, the changes of the molecular conformation and orientation of the adsorbed albumin might also affect platelet adhesion and activation [64, 65]. For the 2738 nm sample and the StrM, the changes of adhered plasma proteins brought by their micron-sized topographical features [75] led to the appearing of round-shaped platelets, as shown in Fig. 7c.

HUVEC adhesion, proliferation, and viability

HUVECs were cultured on different samples for 6 h to evaluate cell adhesion. As shown in Fig. 8a, b, compared to the 2738 nm sample ($14{,}835 \pm 7115$ cells/cm^2), the numbers of adhered HUVECs on the 73 nm sample and the StrM were higher, $20{,}003 \pm 6760$ cells/cm^2 and $18{,}144 \pm 7766$ cells/cm^2, respectively, while there were no significant differences among these samples. Our previous study had demonstrated similar results that the changes in fiber diameter and roughness had no significant influences on HUVEC adhesion [41]. This finding is in agreement with the conclusions from Dong et al., who found that the surface topography (e.g., smooth surface, electrospun fibers with different diameters) did not affect HUVEC adhesion at 6 h, though their electrospun fiber samples were random [76]. After biomolecule immobilization, more HUVECs adhered onto the COL-StrM ($23{,}500 \pm 7829$ cells/cm^2) and the LAM-StrM ($24{,}666 \pm 6954$ cells/cm^2), and the number of adhered cells further increased to $28{,}396 \pm 8754$ cells/cm^2 on the BBM, a significant increase in comparison with the StrM. Cells adhere onto biomaterials via integrin proteins (cell transmembrane receptor proteins), which could bind to ECM proteins, such as collagens, fibronectins, and laminins [77, 78]. Therefore, biomolecule immobilization, especially combining collagen IV and laminin together in the present study, could impose bioactivity to the StrM and improve HUVEC adhesion.

In addition, we could find clearly that the attached HUVECs on the 73 nm, 2738 nm, and the StrM samples did not spread actively. The round and dwindle-shaped morphologies from Fig. 8a suggested that the hydrophobic fiber surface of these samples lacked biological conditions, leading to less adhesion and low activation level of HUVECs. Moreover, from the fluorescence images, HUVECs spread better on the 73 nm sample and the StrM than on the 2738 nm sample. The reason might be that higher surface area could provide more binding sites for HUVECs adhesion and spreading. After biomolecule immobilization, HUVEC spreading improved further with strong expression of F-actin stress fibers, especially on the LAM-StrM and the BBM, demonstrating the positive effects of collagen IV and laminin on HUVEC viability. Of note, HUVECs cultured on the StrM, COL-StrM, LAM-StrM, and BBM aligned along the fiber orientation direction, indicating the strong contact guidance effects of these samples on HUVEC elongation. No obvious HUVEC alignment phenomenon was observed on the 2738 nm sample in the present study, likely because there were less HUVECs adhered for observation, as well as the low activation level of HUVECs, though the aligned microfibers possessed stronger contact guidance effects than the aligned nanofibers [41].

In Fig. 8c, the results of the CCK-8 assay showed that the absorbance exhibited a similar pattern of time-dependent increase in all samples during the culture period. HUVECs on untreated samples (including the 73 nm sample, 2738 nm sample, and StrM) proliferated relatively slowly, while the COL-StrM, LAM-StrM, and BBM exhibited an improved HUVEC proliferation. For the untreated samples, the 73 nm sample always showed the best proliferation situation at 1 d, 3 d, and 5 d because of its similar microstructure with the in vivo environment for HUVECs, with no significant differences with the StrM but significantly better than the 2738 nm sample. It was speculated that the larger surface areas of the 73 nm sample and the StrM provided more binding sites and space for HUVEC adhesion and proliferation. In the meanwhile, protein adhesion might also contribute to the different proliferation situation [41]. Protein adsorbed onto the material surfaces is believed to be the first event after biomaterials were introduced, so that cells would interact with the protein layers, allowing the adsorbed proteins to affect cell behaviors [66, 79]. Moreover, the conformation of the cell adhesion-related proteins (fibronectin and hyponectin) might change the underlying surface properties, which would further affect cell behaviors. It is accepted that micron-sized topographical features promote protein adsorption and unfolding, while smaller nano-sized features provide a more natural surface with less unfavorable protein unfolding [75]. In the present study, the structure of the 2738 nm sample had adverse effects on the conformation of cell adhesion-related proteins, thereby affecting HUVEC proliferation. The StrM was composed of both microfibers and nanofibers, so its negative effects on protein conformation were less than the 2738 nm sample. A similar result has been reported by Amirian et al. who combined oxidized cellulose nanofiber network and PCL fibrous scaffold to develop a unique scaffold, and found that the cyto-compatibility, including cell attachment, viability, and proliferation, of the resultant scaffold significantly improved when compared with the PCL scaffold [80]. Similarly, Luo et al. designed a nano- and sub-micron bacterial cellulose/cellulose acetate scaffold and found it was beneficial for cell migration and proliferation [81].

After biomolecule immobilization, the proliferation of HUVECs on the COL-StrM, LAM-StrM, and BBM

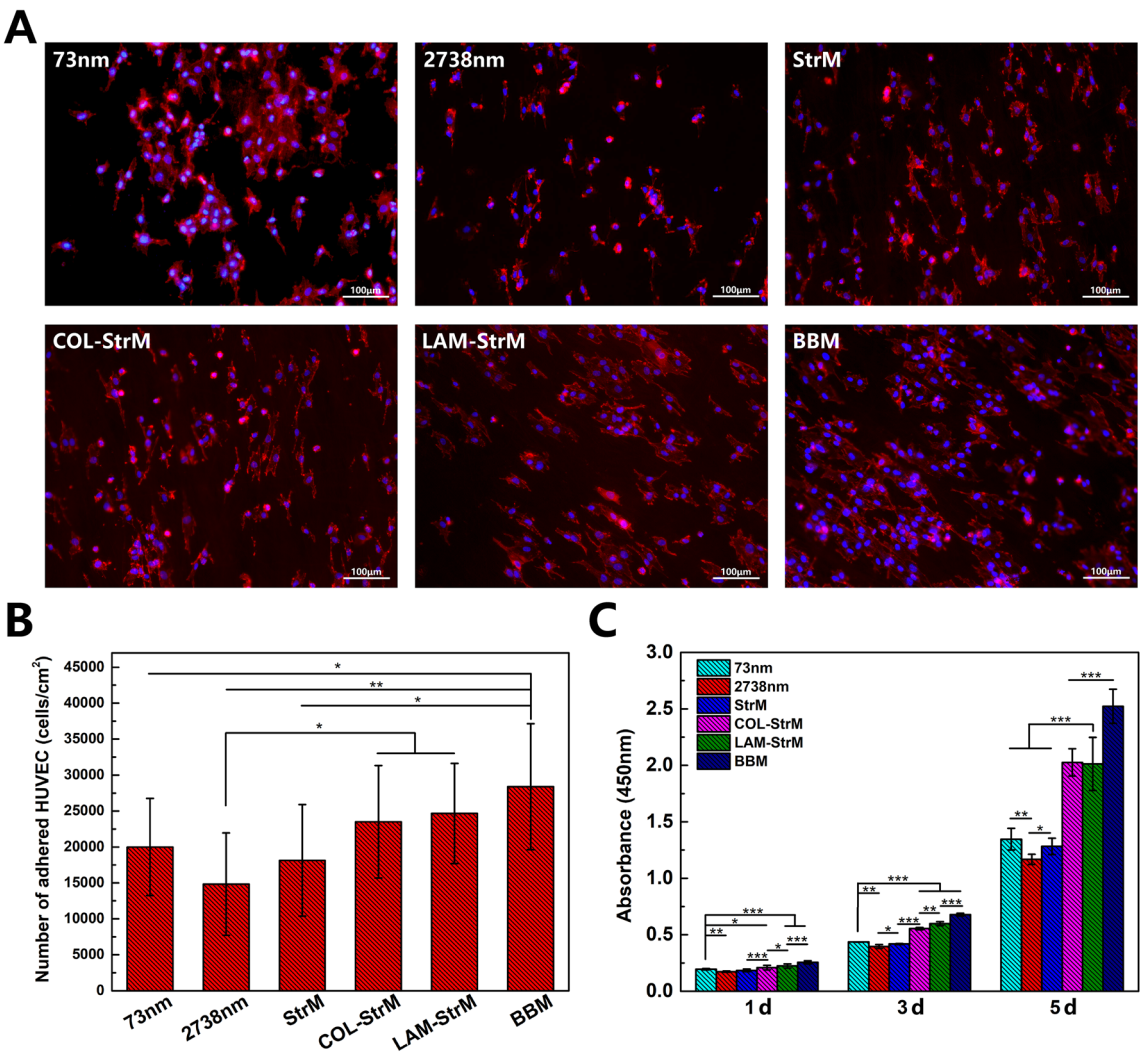

Fig. 8 Fluorescence images (**a**) and numbers (**b**) of adhered HUVECs on different samples at 6 h; **c** statistical results of cell proliferation from the CCK-8 assay at days 1, 3, and 5

improved significantly compared with the untreated samples during the culture period. In Fig. 8c, the BBM showed the best HUVEC proliferation, and the LAM-StrM performed significantly better than the COL-StrM at days 1 and 3, while exhibited similar proliferation level at 5 day. Recall that the microstructures of these three samples were similar, which suggested that the immobilized biomolecules played the dominant role in HUVEC proliferation. As discussed earlier, collagen IV and laminin as the ECM proteins could provide plenty of binding sites for HUVEC adhesion and proliferation [82, 83]. For the BBM, collagen IV and laminin were immobilized simultaneously, leading to the most anchoring sites for HUVEC proliferation, which in turn, produced more cell–cell junctions and promoted rapid endothelialization [84]. Furthermore, it is noteworthy that HUVECs cultured on the LAM-StrM proliferated significantly better than the COL-StrM at days 1 and 3, even though the applied grafting concentration of collagen IV (100 μg/mL) was higher than laminin (20 μg/mL). While further study is warranted, it was speculated that collagen IV lost some of its natural bioactivity during the immobilization process. On the other hand, laminin interacts with integrins and dystroglycan through its globular-like domains, which directly binds to sulfated glycolipids on the cell surface, while little is known about whether collagen IV is directly anchored to cell surfaces [9]. Therefore, in the early stage, the LAM-StrM improved HUVEC proliferation more efficiently than the COL-StrM. In the meanwhile, we inferred that, besides the bioactivity, the quantity of binding domains also played a considerable role in HUVEC proliferation for long-term cell culture. It had been identified that the RGD tripeptide in collagen IV bound with high affinity to integrins [85], so the COL-StrM provided abundant bioactive domains because of the high immobilization concentration of collagen IV, contributing to

its similar HUVEC proliferation level with the LAM-StrM at 5 day.

The viability of the HUVECs was evaluated using a Live/Dead viability kit. As shown in Fig. 9a, HUVECs grew well on all samples at 5 day. Of note, except the 73 nm sample, all other samples allowed HUVEC infiltration, implying their ability to enhance transmural ingrowth for endothelialization. As discussed earlier, transmural capillary ingrowth was essential for confluent vascular graft healing [44]. Hence, besides optimizing EC behaviors for rapid endothelialization, one should also consider to modulate the grafts structures [46, 47, 86] and chemical grafting [44, 48] to improve cell infiltration for increased transmural capillary ingrowth. From the statistical results of cell viability (Fig. 9b), it could be seen that there were no significant differences among the 73 nm, 2738 nm, and StrM samples, meaning that the surface topographies did not affect the HUVEC viability strongly. After biomolecule immobilization, the HUVEC viability was $96.66 \pm 0.98\%$, $98.01 \pm 1.10\%$, and $98.96 \pm 0.89\%$ for the COL-StrM, LAM-StrM, and BBM, respectively, all of which were significantly higher compared with untreated samples. It was because collagen IV and laminin were both vascular BM proteins, providing abundant binding sites for HUVECs adhesion and proliferation [9].

HUVEC morphology

Previous studies had confirmed that elongated ECs showed a better capacity of anti-thrombosis [24] and anti-inflammation [87], as well as more excellent resistance to detachment [38, 88], promoting the formation of a functional endothelium. In Fig. 10a, except the 73 nm sample because of its weak contact guidance effects on HUVEC elongation [41], HUVECs exhibited an elongated morphology along the orientation of the aligned fibers on all other samples. This is in line with the aspect ratio results shown in Fig. 10b. The HUVECs cultured on the 73 nm sample exhibited significant smaller aspect ratios of nuclei than other samples, and the 2738 nm, StrM, COL-StrM, and LAM-StrM samples possessed comparable aspect ratio values with similar contact guidance effects, suggesting that the introduction of nanofibers (compared to the 2738 nm sample) or the immobilization of single biomolecule (compared to the StrM sample) did not affect HUVEC elongation greatly. In the case of the BBM, its value was significantly higher than that of the COL-StrM and LAM-StrM. We speculated that the immobilization of both collagen IV and laminin enhanced the HUVEC activity more strongly, so HUVECs responded to the surface topography more sensitively and intensely. More importantly, except the 73 nm sample, the pores of other five samples in the present study were large enough for HUVEC infiltration (Fig. 10a), and CCK-8 assay evaluated the amount of HUVECs both on and beneath the sample surfaces (Fig. 8c). Therefore, we concluded that the surface of the 73 nm sample promoted the formation of the monolayered HUVEC efficiently, while other five samples allowed HUVEC infiltration, indicating their potential capability for enhancing transmural endothelialization [42–44].

For untreated samples, although the surface topography did have a dramatic effect on HUVEC elongation as indicated by nuclei aspect ratio results, it did not have a statistically significant impact on HUVEC spreading area (cf. Fig. 10c; the 73 nm: $1551.98 \pm 364.58\ \mu m^2$; the 2738 nm: $1658.21 \pm 417.27\ \mu m^2$; the StrM: $1709.42 \pm 979.08\ \mu m^2$). However, Whited et al. demonstrated opposite results that thicker aligned electrospun fibers led to smaller cell coverage areas [38]. After biomolecule immobilization, the average HUVEC spreading areas on the COL-StrM, LAM-StrM, and BBM were $2381.31 \pm 663.84\ \mu m^2$, $3362.35 \pm 696.27\ \mu m^2$, and $2677.45 \pm 763.08\ \mu m^2$, respectively, all significantly higher than that on the untreated samples. This was because the biomolecules provided plenty of focal adhesions sites and thus enhanced adequate cell spreading. In addition, considering that the value of the LAM-StrM was significantly higher than that of the COL-StrM, as well as the lower concentration of laminin (20 μg/mL) than collagen IV (100 μg/mL) during the immobilization process, we concluded that laminin performed better than collagen IV in improving HUVEC spreading. Interestingly, the value of the LAM-StrM was also significantly higher than that of the BBM, which would be explored thoroughly in the future work.

Previous studies had shown that the NSI was affected by the surface topography and stiffness [89, 90], and it increased as the surface confinement grew stronger (e.g., a stiffer or rougher surface, increased surface hydrophilicity), leading to a faster cell migration and rapid endothelialization [43, 91]. In Fig. 10d, the statistical results showed that the 2738 nm sample exhibited a significantly lower average NSI value than all other five samples, and no significant differences could be found among these five samples. A lower NSI value signified a more highly elongated nucleus [91]. In the present study, the HUVECs cultured on the StrM, COL-StrM, LAM-StrM, and BBM exhibited highly elongated nuclei as on the 2738 nm sample (Fig. 10a, b), while average NSI values of them were significantly higher than that of the 2738 nm sample, close to that of the 73 nm sample. We inferred that aligned nanofibers possessed more positive effects on NSI values of the HUVECs than aligned microfibers. Additionally, biomolecule immobilization did not affect NSI values significantly, as the surface topography played the dominant role.

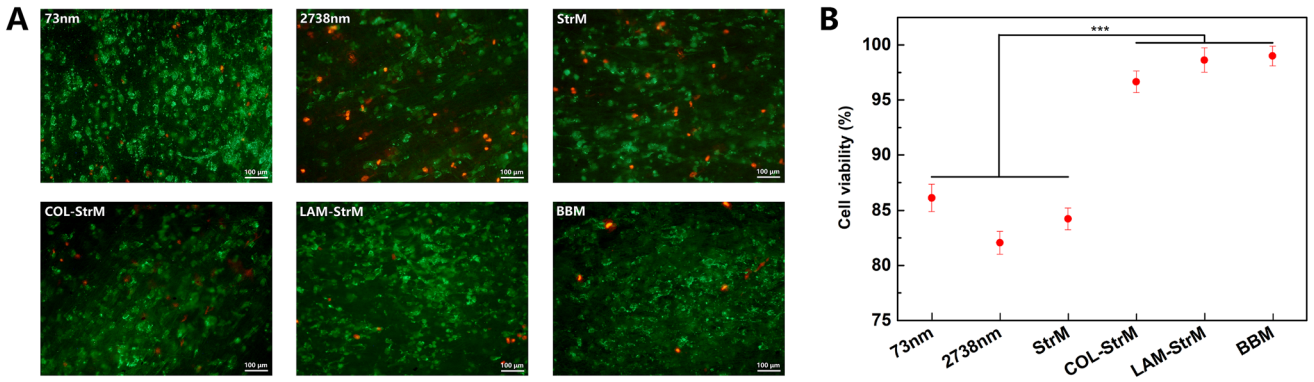

Fig. 9 **a** Live/Dead staining results of HUVECs cultured on different samples; **b** statistical results of cell viability from the Live/Dead assay

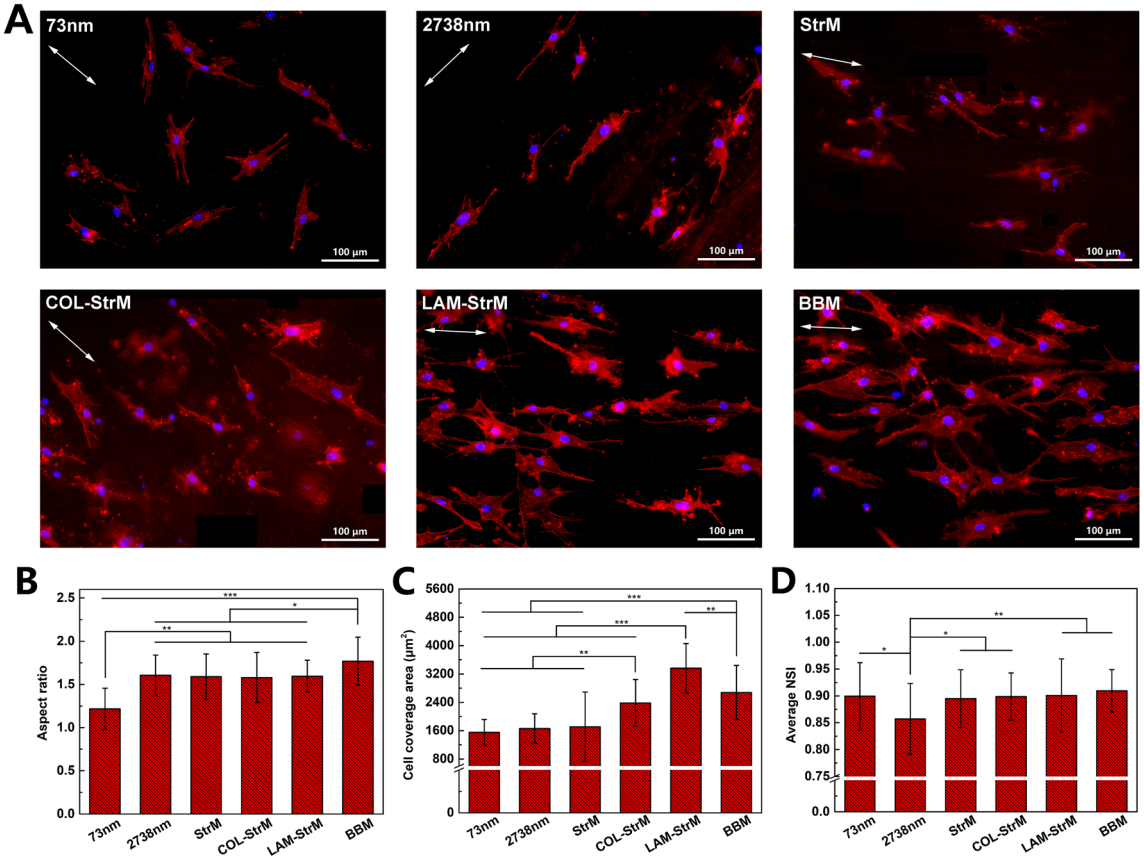

Fig. 10 **a** Fluorescence images of HUVECs cultured on different samples after 3 d incubation. White arrows indicate the direction of the principal axis of the aligned fibers; quantitative analysis of the aspect ratio of the nucleus (**b**), the cell coverage area (**c**), and the average NSI (**d**) of the HUVECs

NO and PGI2 production

NO is a key physiological molecule secreted by ECs, acting as a signaling cytokine to regulate the ECs, SMCs, and macrophages behaviors [75], and playing a significant role in preventing platelet adhesion and aggregation [53, 54]. PGI2 is another cytokine secreted by the ECs, with similar functions to NO in inhibiting thrombus formation and excessive proliferation of the SMCs [92]. Both NO and PGI2 have long been recognized for their capability to maintain the long-term patency of small-diameter vascular grafts.

In Fig. 11, it could be seen that there were no significant differences among the normalized NO and PGI2 concentrations of untreated samples, suggesting that the morphology elongation (induced by different surface topographies) did not significantly affect NO and PGI2 release capability of sin-

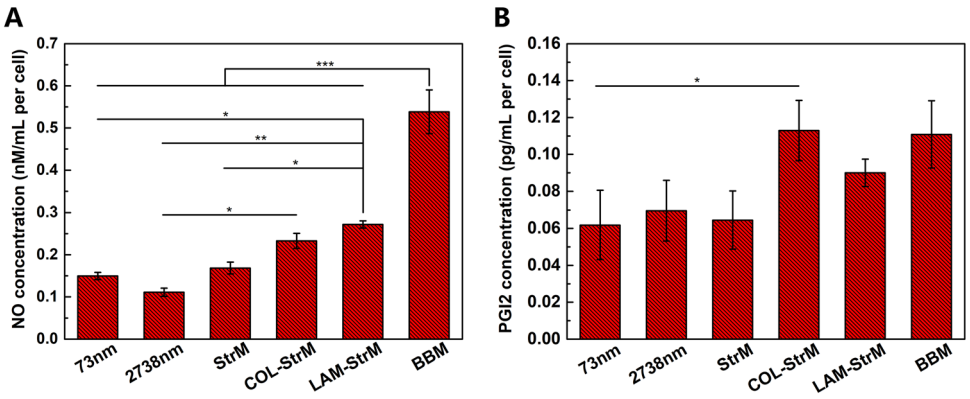

Fig. 11 Concentration of normalized NO (**a**) and PGI2 (**b**) released by the HUVECs cultured on different samples

gle HUVEC. It should be pointed out that some studies had shown that the elongated ECs induced by blood flow shear stress or structure cues possessed higher cell activity and released more functional factors [93–95]. After biomolecule immobilization, NO concentration values increased greatly, especially for the LAM-StrM and BBM, and their values were significantly higher than that of untreated samples. The BBM had the highest value of 0.5384 ± 0.0517 nM/mL per cell, a significant improvement compared with the LAM-StrM of 0.2719 ± 0.0084 nM/mL per cell (Fig. 11a). And, as presented in Fig. 11b, the biomolecules seemed to play an auxiliary catalytic role for HUVEC's PGI2 secretion, because the PGI2 concentration values of the COL-StrM, LAM-StrM, and BBM were higher than that of untreated samples, even though it made no significant contribution directly. Altogether, biomolecules played a crucial role in modulating NO and PGI2 production of HUVECs as previous reported [96–98]. More importantly, taking the HUVEC proliferation results into consideration (cf. Fig. 8c), the BBM exhibited the highest NO and PGI2 secretion amounts of HUVECs, demonstrating its best antithrombotic property, which was beneficial for long-term patency of small-diameter vascular implants.

Conclusions

In this study, we developed a bio-inspired BBM by immobilizing natural ECM proteins, i.e., collagen IV and laminin, onto an aligned nano/microfibrous scaffold for promoting rapid endothelialization. Hemocompatibility results showed that the BBM exhibited satisfactory blood compatibility and enhanced inhibition of platelet adhesion and activation. The HUVEC behaviors, including adhesion, proliferation, spreading, and migration, indicated that the BBM possessed both the positive contact guidance effects of aligned nano- and microfibers, and the improved HUVEC affinity of immobilized collagen IV and laminin. Of note, the BBM possessed desirable pore structure for HUVEC infiltration, which was beneficial for transmural endothelialization. In addition, the BBM exhibited improved antithrombotic capability as indicated by higher expression of NO and PGI2 secretion. Altogether, the BBM with hierarchical structures and instructive ECM proteins combined simultaneous biophysical and biochemical cues to promote rapid endothelialization and maintain the long-term patency for small-diameter vascular implants.

Acknowledgements This work was supported by the Fundamental Research Funds for the Central Universities (Nos. 2232019G-06 and 2232019A3-06) and 111 project (No. PB0719035). The authors at University of Wisconsin-Madison would like to acknowledge the partial support by the Wisconsin Institute for Discovery (WID), the NHLBI of the National Institutes of Health (No. U01HL134655), and the Kuo K. and Cindy F. Wang Professorship. Chenglong Yu also acknowledged the fellowship from the China Scholarship Council (CSC) under the Grant CSC No. 201906630070.

Author contributions Conceptualization, CY and GG; Methodology, CY and LT; Investigation, CY, ZL and SG; Writing-Original Draft, CY and LW; Writing-Review & Editing, LT, LW and GG; Funding Acquisition, LW, LT and CY.

Compliance with ethical standards

Conflict of interest The authors declare that they have no conflict of interest.

Ethical approval This study does not contain any studies with human or animal subjects performed by any of the authors.

References

1. Radke D, Jia WK, Sharma D, Fena K, Wang GF, Goldman J, Zhao F (2018) Tissue engineering at the blood-contacting surface: a review of challenges and strategies in vascular graft development. Adv Healthc Mater 7(15):1701461. https://doi.org/10.1002/adhm.201701461
2. Kurobe H, Maxfield MW, Breuer CK, Shinoka T (2012) Concise review: tissue-engineered vascular grafts for cardiac surgery: past, present, and future. Stem Cells Transl Med 1(7):566–571. https://doi.org/10.5966/sctm.2012-0044

3. Mi HY, Jing X, Thomsom JA, Turng LS (2018) Promoting endothelial cell affinity and antithrombogenicity of polytetrafluoroethylene (PTFE) by mussel-inspired modification and RGD/heparin grafting. J Mater Chem B 6(21):3475–3485. https://doi.org/10.1039/c8tb00654g
4. Gao A, Hang RQ, Li W, Zhang W, Li PH, Wang GM, Bai L, Yu XF, Wang HY, Tong LP, Chu PK (2017) Linker-free covalent immobilization of heparin, SDF-1 alpha, and CD47 on PTFE surface for antithrombogenicity, endothelialization and anti-inflammation. Biomaterials 140:201–211. https://doi.org/10.1016/j.biomaterials.2017.06.023
5. Yalcin I, Horakova J, Mikes P, Sadikoglu TG, Domin R, Lukas D (2016) Design of polycaprolactone vascular grafts. J Ind Text 45(5):813–833. https://doi.org/10.1177/1528083714540701
6. Shireman PK, Pearce WH (1996) Endothelial cell function: Biologic and physiologic functions in health and disease. Am J Roentgenol 166(1):7–13. https://doi.org/10.2214/ajr.166.1.8571908
7. Babitha S, Rachita L, Karthikeyan K, Shoba E, Janani I, Poornima B, Sai KP (2017) Electrospun protein nanofibers in healthcare: a review. Int J Pharmaceut 523(1):52–90. https://doi.org/10.1016/j.ijpharm.2017.03.013
8. Cahill PA, Redmond EM (2016) Vascular endothelium—gatekeeper of vessel health. Atherosclerosis 248:97–109. https://doi.org/10.1016/j.atherosclerosis.2016.03.007
9. Jayadev R, Sherwood DR (2017) Basement membranes. Curr Biol 27(6):R207–R211. https://doi.org/10.1016/j.cub.2017.02.006
10. Ren XK, Feng YK, Guo JT, Wang HX, Li Q, Yang J, Hao XF, Lv J, Ma N, Li WZ (2015) Surface modification and endothelialization of biomaterials as potential scaffolds for vascular tissue engineering applications. Chem Soc Rev 44(15):5680–5742. https://doi.org/10.1039/c4cs00483c
11. L'Heureux N, Dusserre N, Konig G, Victor B, Keire P, Wight TN, Chronos NAF, Kyles AE, Gregory CR, Hoyt G, Robbins RC, McAllister TN (2006) Human tissue-engineered blood vessels for adult arterial revascularization. Nat Med 12(3):361–365. https://doi.org/10.1038/nm1364
12. Kruger-Genge A, Fuhrmann R, Jung F, Franke RP (2016) Effects of different components of the extracellular matrix on endothelialization. Clin Hemorheol Microcirc 64(4):867–874. https://doi.org/10.3233/ch-168051
13. Anderson DEJ, Truong KP, Hagen MW, Yim EKF, Hinds MT (2019) Biomimetic modification of poly(vinyl alcohol): Encouraging endothelialization and preventing thrombosis with antiplatelet monotherapy. Acta Biomater 86:291–299. https://doi.org/10.1016/j.actbio.2019.01.008
14. Ardila DC, Liou J-J, Maestas D, Slepian MJ, Badowski M, Wagner W, Harris D, Vande Geest JP (2019) Surface modification of electrospun scaffolds for endothelialization of tissue-engineered vascular grafts using human cord blood-derived endothelial cells. J Clin Med 8(2):185. https://doi.org/10.3390/jcm8020185
15. Holland I, Logan J, Shi JZ, McCormick C, Liu DS, Shu WM (2018) 3D biofabrication for tubular tissue engineering. Bio-Des Manuf 1(2):89–100. https://doi.org/10.1007/s42242-018-0013-2
16. Liliensiek SJ, Nealey P, Murphy CJ (2009) Characterization of endothelial basement membrane nanotopography in rhesus macaque as a guide for vessel tissue engineering. Tissue Eng A 15(9):2643–2651. https://doi.org/10.1089/ten.tea.2008.0284
17. Han JJ, Gerstenhaber JA, Lazarovici P, Lelkes PI (2013) Tissue factor activity and ECM-related gene expression in human aortic endothelial cells grown on electrospun biohybrid scaffolds. Biomacromol 14(5):1338–1348. https://doi.org/10.1021/bm400450m
18. Davis GE, Senger DR (2005) Endothelial extracellular matrix - Biosynthesis, remodeling, and functions during vascular morphogenesis and neovessel stabilization. Circ Res 97(11):1093–1107. https://doi.org/10.1161/01.RES.0000191547.64391.e3
19. Pozzi A, Yurchenco PD, Lozzo RV (2017) The nature and biology of basement membranes. Matrix Biol 57–58:1–11. https://doi.org/10.1016/j.matbio.2016.12.009
20. Brody S, Anilkumar T, Liliensiek S, Last JA, Murphy CJ, Pandit A (2006) Characterizing nanoscale topography of the aortic heart valve basement membrane for tissue engineering heart valve scaffold design. Tissue Eng 12(2):413–421. https://doi.org/10.1089/ten.2006.12.413
21. Kalluri R (2003) Basement membranes: Structure, assembly and role in tumour angiogenesis. Nat Rev Cancer 3(6):422–433. https://doi.org/10.1038/nrc1094
22. Dankers PYW, Boomker JM, Huizinga-van der Vlag A, Wisse E, Appel WPJ, Smedts FMM, Harmsen MC, Bosman AW, Meijer W, van Luyn MJA (2011) Bioengineering of living renal membranes consisting of hierarchical, bioactive supramolecular meshes and human tubular cells. Biomaterials 32(3):723–733. https://doi.org/10.1016/j.biomaterials.2010.09.020
23. Murikipudi S, Methe H, Edelman ER (2013) The effect of substrate modulus on the growth and function of matrix-embedded endothelial cells. Biomaterials 34(3):677–684. https://doi.org/10.1016/j.biomaterials.2012.09.079
24. Chen JY, Hu M, Zhang H, Li BC, Chang H, Ren KF, Wang YB, Ji J (2018) Improved antithrombotic function of oriented endothelial cell monolayer on microgrooves. ACS Biomater Sci Eng 4(6):1976–1985. https://doi.org/10.1021/acsbiomaterials.7b00496
25. Ye CR, Wang Y, Su H, Yang P, Huang N, Maitz MF, Zhao AS (2016) Construction of a fucoidan/laminin functional multilayer to direction vascular cell fate and promotion hemocompatibility. Mater Sci Eng C Mater 64:236–242. https://doi.org/10.1016/j.msec.2016.03.070
26. Palotie A, Tryggvason K, Peltonen L, Seppa H (1983) Components of subendothelial aorta basement membrane. Immunohistochemical localization and role in cell attachment. Lab Investig 49(3):362–370
27. Form DM, Pratt BM, Madri JA (1986) Endothelial cell proliferation during angiogenesis. In vitro modulation by basement membrane components. Lab Investig 55(5):521–530
28. Aird WC (2007a) Phenotypic heterogeneity of the endothelium II. Representative vascular beds. Circ Res 100(2):174–190. https://doi.org/10.1161/01.RES.0000255690.03436.ae
29. Aird WC (2007b) Phenotypic heterogeneity of the endothelium I. Structure, function, and mechanisms. Circ Res 100(2):158–173. https://doi.org/10.1161/01.RES.0000255691.76142.4a
30. Schwarz US, Balaban NQ, Riveline D, Bershadsky A, Geiger B, Safran SA (2002) Calculation of forces at focal adhesions from elastic substrate data: the effect of localized force and the need for regularization. Biophys J 83(3):1380–1394. https://doi.org/10.1016/s0006-3495(02)73909-x
31. Heath DE (2017) Promoting endothelialization of polymeric cardiovascular biomaterials. Macromol Chem Phys 218(8):UNSP1600574. https://doi.org/10.1002/macp.201600574
32. Shin YM, Shin HJ, Heo Y, Jun I, Chung YW, Kim K, Lim YM, Jeon H, Shin H (2017) Engineering an aligned endothelial monolayer on a topologically modified nanofibrous platform with a micropatterned structure produced by femtosecond laser ablation. J Mater Chem B 5(2):318–328. https://doi.org/10.1039/c6tb02258h
33. Mott RE, Helmke BP (2007) Mapping the dynamics of shear stress-induced structural changes in endothelial cells. Am J Physiol Cell Physiol 293(5):C1616–C1626. https://doi.org/10.1152/ajpcell.00457.2006
34. Nikkhah M, Edalat F, Manoucheri S, Khademhosseini A (2012) Engineering microscale topographies to control the cell-substrate

interface. Biomaterials 33(21):5230–5246. https://doi.org/10.1016/j.biomaterials.2012.03.079
35. Nivison-Smith L, Weiss AS (2012) Alignment of human vascular smooth muscle cells on parallel electrospun synthetic elastin fibers. J Biomed Mater Res A 100A(1):155–161. https://doi.org/10.1002/jbm.a.33255
36. Wang YC, Wang Y, Mei DQ, Yu ZK, Xue D (2020) Standing surface acoustic wave-assisted fabrication of patterned microstructures for enhancing cell migration. Bio-Des Manuf 3(2):87–97. https://doi.org/10.1007/s42242-020-00071-x
37. Zhong J, Zhang H, Yan J, Gong X (2015) Effect of nanofiber orientation of electrospun nanofibrous scaffolds on cell growth and elastin expression of muscle cells. Colloid Surf B 136:772–778. https://doi.org/10.1016/j.colsurfb.2015.10.017
38. Whited BM, Rylander MN (2014) The influence of electrospun scaffold topography on endothelial cell morphology, alignment, and adhesion in response to fluid flow. Biotechnol Bioeng 111(1):184–195. https://doi.org/10.1002/bit.24995
39. Li XY, Wang XF, Yao DS, Jiang J, Guo X, Gao YH, Li Q, Shen CY (2018) Effects of aligned and random fibers with different diameter on cell behaviors. Colloid Surf B 171:461–467. https://doi.org/10.1016/j.colsurfb.2018.07.045
40. Yu CL, Xing MY, Sun SB, Guan GP, Wang L (2019) In vitro evaluation of vascular endothelial cell behaviors on biomimetic vascular basement membranes. Colloid Surf B 182:UNSP110381. https://doi.org/10.1016/j.colsurfb.2019.110381
41. Yu CL, Xing MY, Wang L, Guan GP (2020) Effects of aligned electrospun fibers with different diameters on hemocompatibility, cell behaviors and inflammation in vitro. Biomed Mater 15(3):035005. https://doi.org/10.1088/1748-605X/ab673c
42. Zhang Z, Wang ZX, Liu SQ, Kodama M (2004) Pore size, tissue ingrowth, and endothelialization of small-diameter microporous polyurethane vascular prostheses. Biomaterials 25(1):177–187. https://doi.org/10.1016/s0142-9612(03)00478-2
43. Sanchez PF, Brey EM, Briceno JC (2018) Endothelialization mechanisms in vascular grafts. J Tissue Eng Regen M 12:2164–2178. https://doi.org/10.1002/term.2747
44. Pennel T, Bezuidenhout D, Koehne J, Davies NH, Zilla P (2018) Transmural capillary ingrowth is essential for confluent vascular graft healing. Acta Biomater 65:237–247. https://doi.org/10.1016/j.actbio.2017.10.038
45. Pennel T, Zilla P, Bezuidenhout D (2013) Differentiating transmural from transanastomotic prosthetic graft endothelialization through an isolation loop-graft model. J Vasc Surg 58(4):1053–1061. https://doi.org/10.1016/j.jvs.2012.11.093
46. Eichhorn SJ, Sampson WW (2005) Statistical geometry of pores and statistics of porous nanofibrous assemblies. J R Soc Interface 2(4):309–318. https://doi.org/10.1098/rsif.2005.0039
47. Pham QP, Sharma U, Mikos AG (2006) Electrospun poly(epsilon-caprolactone) microfiber and multilayer nanofiber/microfiber scaffolds: characterization of scaffolds and measurement of cellular infiltration. Biomacromol 7(10):2796–2805. https://doi.org/10.1021/bm060680j
48. Bezuidenhout D, Davies N, Black M, Schmidt C, Oosthuysen A, Zilla P (2010) Covalent surface heparinization potentiates porous polyurethane scaffold vascularization. J Biomater Appl 24(5):401–418. https://doi.org/10.1177/0885328208097565
49. Drevelle O, Bergeron E, Senta H, Lauzon MA, Roux S, Grenier G, Faucheux N (2010) Effect of functionalized polycaprolactone on the behaviour of murine preosteoblasts. Biomaterials 31(25):6468–6476. https://doi.org/10.1016/j.biomaterials.2010.05.010
50. Zhu JJ, Chen D, Du J, Chen XX, Wang JH, Zhang HB, Chen SH, Wu JL, Zhu TH, Mo XM (2020) Mechanical matching nanofibrous vascular scaffold with effective anticoagulation for vascular tissue engineering. Compos B Eng 186:107788. https://doi.org/10.1016/j.compositesb.2020.107788
51. Wang DF, Wang XF, Zhang Z, Wang LX, Li XM, Xu YY, Ren CH, Li Q, Turng LS (2019) Programmed release of multimodal, cross-linked vascular endothelial growth factor and heparin layers on electrospun polycaprolactone vascular grafts. ACS Appl Mater Int 11(35):32533–32542. https://doi.org/10.1021/acsami.9b10621
52. Guo X, Wang X, Li X, Jiang Y-C, Han S, Ma L, Guo H, Wang Z, Li Q (2020) Endothelial cell migration on poly(epsilon-caprolactone) nanofibers coated with a nanohybrid Shish-Kebab structure mimicking collagen fibrils. Biomacromol 21(3):1202–1213. https://doi.org/10.1021/acs.biomac.9b01638
53. Forstermann U, Xia N, Li HG (2017) Roles of vascular oxidative stress and nitric oxide in the pathogenesis of atherosclerosis. Circ Res 120(4):713–735. https://doi.org/10.1161/circresaha.116.309326
54. Zhao YZ, Vanhoutte PM, Leung SWS (2015) Vascular nitric oxide: beyond eNOS. J Pharmacol Sci 129(2):83–94. https://doi.org/10.1016/j.jphs.2015.09.002
55. Han CZ, Luo X, Zou D, Li JA, Zhang K, Yang P, Huang N (2019) Nature-inspired extracellular matrix coating produced by micro-patterned smooth muscle and endothelial cells endows cardiovascular materials with better biocompatibility. Biomater Sci 7(7):2686–2701. https://doi.org/10.1039/c9bm00128j
56. Al Faouri R, Henry R, Biris AS, Sleezer R, Salamo GJ (2017) Adhesive force between graphene nanoscale flakes and living biological cells. J Appl Toxicol 37(11):1346–1353. https://doi.org/10.1002/jat.3478
57. Bae YI, Hwang I, Kim I, Kim K, Park JW (2017) Force measurement for the interaction between cucurbit 7 uril and mica and self-assembled monolayer in the presence of Zn^{2+} studied with atomic force microscopy. Langmuir 33(43):11884–11892. https://doi.org/10.1021/acs.langmuir.7b02168
58. Baker SR, Banerjee S, Bonin K, Guthold M (2016) Determining the mechanical properties of electrospun poly-epsilon-caprolactone (PCL) nanofibers using AFM and a novel fiber anchoring technique. Mat Sci Eng C Mater 59:203–212. https://doi.org/10.1016/j.msec.2015.09.102
59. Li Y, Xiao ZC, Zhou YJ, Zheng S, An Y, Huang W, He HC, Yang Y, Li SY, Chen YX, Xiao J, Wu J (2019) Controlling the multiscale network structure of fibers to stimulate wound matrix rebuilding by fibroblast differentiation. ACS Appl Mater Int 11(31):28377–28386. https://doi.org/10.1021/acsami.9b06439
60. Lichtenberg A, Tudorache I, Cebotari S, Ringes-Lichtenberg S, Sturz G, Hoeffler K, Hurscheler C, Brandes G, Hilfiker A, Haverich A (2006) In vitro re-endothelialization of detergent decellularized heart valves under simulated physiological dynamic conditions. Biomaterials 27(23):4221–4229. https://doi.org/10.1016/j.biomaterials.2006.03.047
61. Ghobeira R, Philips C, Liefooghe L, Verdonck M, Asadian M, Cools P, Declercq H, De Vos WH, De Geyter N, Morent R (2019) Synergetic effect of electrospun PCL fiber size, orientation and plasma-modified surface chemistry on stem cell behavior. Appl Surf Sci 485:204–221. https://doi.org/10.1016/j.apsusc.2019.04.109
62. Milleret V, Hefti T, Hall H, Vogel V, Eberli D (2012) Influence of the fiber diameter and surface roughness of electrospun vascular grafts on blood activation. Acta Biomater 8(12):4349–4356. https://doi.org/10.1016/j.actbio.2012.07.032
63. Venault A, Ballad MRB, Liu YH, Aimar P, Chang Y (2015) Hemocompatibility of PVDF/PS-b-PEGMA membranes prepared by LIPS process. J Membr Sci 477:101–114. https://doi.org/10.1016/j.memsci.2014.12.024
64. Jeyachandran YL, Mielezarski E, Rai B, Mielczarski JA (2009) Quantitative and qualitative evaluation of adsorption/desorption of bovine serum albumin on hydrophilic and hydrophobic surfaces.

Langmuir 25(19):11614–11620. https://doi.org/10.1021/la901453a
65. Rodrigues SN, Goncalves IC, Martins MCL, Barbosa MA, Ratner BD (2006) Fibrinogen adsorption, platelet adhesion and activation on mixed hydroxyl-/methyl-terminated self-assembled monolayers. Biomaterials 27(31):5357–5367. https://doi.org/10.1016/j.biomaterials.2006.06.010
66. Arima Y, Iwata H (2007) Effect of wettability and surface functional groups on protein adsorption and cell adhesion using well-defined mixed self-assembled monolayers. Biomaterials 28(20):3074–3082. https://doi.org/10.1016/j.biomaterials.2007.03.013
67. Wu Y, Yu C, Xing M, Wang L, Guan G (2019) Surface modification of polyvinyl alcohol (PVA)/polyacrylamide (PAAm) hydrogels with polydopamine and REDV for improved applicability. J Biomed Mater Res B 108:117–127. https://doi.org/10.1002/jbm.b.34371
68. Modi A, Verma SK, Bellare J (2018) Extracellular matrix-coated polyethersulfone-TPGS hollow fiber membranes showing improved biocompatibility and uremic toxins removal for bioartificial kidney application. Colloid Surf B 167:457–467. https://doi.org/10.1016/j.colsurfb.2018.04.043
69. Zilla P, Bezuidenhout D, Human P (2007) Prosthetic vascular grafts: wrong models, wrong questions and no healing. Biomaterials 28(34):5009–5027. https://doi.org/10.1016/j.biomaterials.2007.07.017
70. Elbaz A, He ZZ, Gao BB, Chi JJ, Su EB, Zhang DG, Liu SQ, Xu H, Liu H, Gu ZZ (2018) Recent biomedical applications of biosourced materials. Bio-Des Manuf 1(1):26–44. https://doi.org/10.1007/s42242-018-0002-5
71. Sandmann R, Koster S (2016) Topographic cues reveal two distinct spreading mechanisms in blood platelets. Sci Rep 6:22357. https://doi.org/10.1038/srep22357
72. Bae S, DiBalsi MJ, Meilinger N, Zhang CQ, Beal E, Korneva G, Brown RO, Kornev KG, Lee JS (2018) Heparin-eluting electrospun nanofiber yarns for antithrombotic vascular sutures. ACS Appl Mater Int 10(10):8426–8435. https://doi.org/10.1021/acsami.7b14888
73. Zhang K, Li JA, Deng K, Liu T, Chen JY, Huang N (2013) The endothelialization and hemocompatibility of the functional multilayer on titanium surface constructed with type IV collagen and heparin. Colloid Surf B 108:295–304. https://doi.org/10.1016/j.colsurfb.2012.12.053
74. White-Adams TC, Berny MA, Patel IA, Tucker EI, Gailani D, Gruber A, McCarty OJT (2010) Laminin promotes coagulation and thrombus formation in a factor XII-dependent manner. J Thromb Haemost 8(6):1295–1301. https://doi.org/10.1111/j.1538-7836.2010.03850.x
75. Lavery KS, Rhodes C, McGraw A, Eppihimer MJ (2017) Antithrombotic technologies for medical devices. Adv Drug Deliv Rev 112:2–11. https://doi.org/10.1016/j.addr.2016.07.008
76. Dong XH, Yuan XY, Wang LN, Liu JL, Midgley AC, Wang ZH, Wang K, Liu JF, Zhu MF, Kong DL (2018) Construction of a bilayered vascular graft with smooth internal surface for improved hemocompatibility and endothelial cell monolayer formation. Biomaterials 181:1–14. https://doi.org/10.1016/j.biomaterials.2018.07.027
77. Bruinink A, Bitar M, Pleskova M, Wick P, Krug HF, Maniura-Weber K (2014) Addition of nanoscaled bioinspired surface features: a revolution for bone-related implants and scaffolds? J Biomed Mater Res A 102(1):275–294. https://doi.org/10.1002/jbm.a.34691
78. Koivisto L, Bi JR, Hakkinen L, Larjava H (2018) Integrin alpha v beta 6: Structure, function and role in health and disease. Int J Biochem Cell Biol 99:186–196. https://doi.org/10.1016/j.biocel.2018.04.013
79. Skoog SA, Kumar G, Narayan RJ, Goering PL (2018) Biological responses to immobilized microscale and nanoscale surface topographies. Pharmacol Ther 182:33–55. https://doi.org/10.1016/j.pharmthera.2017.07.009
80. Amirian J, Lee SY, Lee BT (2016) Designing of combined nano and microfiber network by immobilization of oxidized cellulose nanofiber on polycaprolactone fibrous scaffold. J Biomed Nanotechnol 12(10):1864–1875. https://doi.org/10.1166/jbn.2016.2308
81. Luo HL, Gan DQ, Gama M, Tu JP, Yao FL, Zhang QC, Ao HY, Yang ZW, Li JJ, Wan YZ (2020) Interpenetrated nano- and submicrofibrous biomimetic scaffolds towards enhanced mechanical and biological performances. Mater Sci Eng C Mater 108:110416. https://doi.org/10.1016/j.msec.2019.110416
82. Heo Y, Shin YM, Bin Lee Y, Lim YM, Shin H (2015) Effect of immobilized collagen type IV on biological properties of endothelial cells for the enhanced endothelialization of synthetic vascular graft materials. Colloid Surf B 134:196–203. https://doi.org/10.1016/j.colsurfb.2015.07.003
83. Koh HS, Yong T, Chan CK, Ramakrishna S (2008) Enhancement of neurite outgrowth using nano-structured scaffolds coupled with laminin. Biomaterials 29(26):3574–3582. https://doi.org/10.1016/j.biomaterials.2008.05.014
84. Li MY, Mondrinos MJ, Gandhi MR, Ko FK, Weiss AS, Lelkes PI (2005) Electrospun protein fibers as matrices for tissue engineering. Biomaterials 26(30):5999–6008. https://doi.org/10.1016/j.biomaterials.2005.03.030
85. Zhang Z, Lai YX, Yu L, Ding JD (2010) Effects of immobilizing sites of RGD peptides in amphiphilic block copolymers on efficacy of cell adhesion. Biomaterials 31(31):7873–7882. https://doi.org/10.1016/j.biomaterials.2010.07.014
86. Tang FY, Manz XD, Bongers A, Odell RA, Joukhdar H, Whitelock JM, Lord MS, Rnjak-Kovacina J (2020) Microchannels are an architectural cue that promotes integration and vascularization of silk biomaterials in vivo. ACS Biomater Sci Eng 6(3):1476–1486. https://doi.org/10.1021/acsbiomaterials.9b01624
87. Chiu JJ, Usami S, Chien S (2009) Vascular endothelial responses to altered shear stress: pathologic implications for atherosclerosis. Ann Med 41(1):19–28. https://doi.org/10.1080/07853890802186921
88. Inoguchi H, Tanaka T, Maehara Y, Matsuda T (2007) The effect of gradually graded shear stress on the morphological integrity of a HUVEC-seeded compliant small-diameter vascular graft. Biomaterials 28(3):486–495. https://doi.org/10.1016/j.biomaterials.2006.09.020
89. van Helvert S, Storm C, Friedl P (2018) Mechanoreciprocity in cell migration. Nat Cell Biol 20(1):8–20. https://doi.org/10.1038/s41556-017-0012-0
90. Sheets K, Wunsch S, Ng C, Nain AS (2013) Shape-dependent cell migration and focal adhesion organization on suspended and aligned nanofiber scaffolds. Acta Biomater 9(7):7169–7177. https://doi.org/10.1016/j.actbio.2013.03.042
91. Meehan S, Nain AS (2014) Role of suspended fiber structural stiffness and curvature on single-cell migration, nucleus shape, and focal-adhesion-cluster length. Biophys J 107(11):2604–2611. https://doi.org/10.1016/j.bpj.2014.09.045
92. Li JG, Zhang K, Yang P, Qin W, Li GC, Zhao AS, Huang N (2013) Human vascular endothelial cell morphology and functional cytokine secretion influenced by different size of HA micro-pattern on titanium substrate. Colloid Surf B 110:199–207. https://doi.org/10.1016/j.colsurfb.2013.04.048
93. Cutiongco MFA, Goh SH, Aid-Launais R, Le Visage C, Low HY, Yim EKF (2016) Planar and tubular patterning of micro and nano-topographies on poly(vinyl alcohol) hydrogel for improved endothelial cell responses. Biomaterials 84:184–195. https://doi.org/10.1016/j.biomaterials.2016.01.036

94. Morgan JT, Wood JA, Shah NM, Hughbanks ML, Russell P, Barakat AI, Murphy CJ (2012) Integration of basal topographic cues and apical shear stress in vascular endothelial cells. Biomaterials 33(16):4126–4135. https://doi.org/10.1016/j.biomaterials.2012.02.047
95. Gong XH, Yao J, He HP, Zhao XX, Liu XY, Zhao F, Sun Y, Fan YB (2017) Combination of flow and micropattern alignment affecting flow-resistant endothelial cell adhesion. J Mech Behav Biomed 74:11–20. https://doi.org/10.1016/j.jmbbm.2017.04.028
96. Post A, Wang E, Cosgriff-Hernandez E (2019) A review of integrin-mediated endothelial cell phenotype in the design of cardiovascular devices. Ann Biomed Eng 47(2):366–380. https://doi.org/10.1007/s10439-018-02171-3
97. Balcells M, Edelman ER (2002) Effect of pre-adsorbed proteins on attachment, proliferation, and function of endothelial cells. J Cell Physiol 191(2):155–161. https://doi.org/10.1002/jcp.10087
98. Lu A, Sipehia R (2001) Antithrombotic and fibrinolytic system of human endothelial cells seeded on PTFE: the effects of surface modification of PTFE by ammonia plasma treatment and ECM protein coatings. Biomaterials 22(11):1439–1446. https://doi.org/10.1016/s0142-9612(00)00302-1